A Novel Asymmetric Interior Permanent Magnet Machine for Electric Vehicles

Y. Xiao ⬤, Z. Q. Zhu ⬤, *Fellow, IEEE*, S. S. Wang, G. W. Jewell ⬤, J. T. Chen, *Senior Member, IEEE*, D. Wu, and L. M. Gong

Abstract—A novel asymmetric interior permanent magnet (AIPM) machine is proposed in this paper for electric vehicle application. It has a skewed V-shape permanent magnet (PM) cavity, two PMs with different dimensions and an additional flux barrier outside the V-shape cavity in each pole. This asymmetric rotor topology can inherently utilize the magnetic-field-shifting (MFS) effect to reduce the current angle difference between the maximum PM and reluctance torque components, thereby enhancing the maximum synthetic torque with the same PM usage. The influences of cavity positions in the proposed AIPM and an existing AIPM with extra flux barrier inside the V-shape cavity are investigated and compared using finite element analysis. It is found that the proposed structure with outside flux barrier has higher average torque than the one with inside flux barrier. Both AIPM topologies are designed with the same stator, rotor diameter, and PM usage as the conventional V-shape IPM benchmark for Prius 2010. Electromagnetic, mechanical and steady-state thermal performance of three machines are compared. The results confirm that the proposed AIPM machine can achieve significant torque enhancement due to utilizing MFS effect, compared with the existing AIPM and the IPM benchmark. Finally, a small prototype of the proposed AIPM machine is designed, manufactured and tested to validate the FE analysis.

Index Terms—Asymmetric interior permanent magnet (AIPM), flux barrier, electric vehicle, magnetic-field shifting (MFS) effect, reluctance torque.

NOMENCLATURE

B_{res}	Residual magnetism of PM material, T
B_g	Air-gap flux density, T
$b_{cl}, b_{cr}, b_{ol}, b_{oc}, b_{or}$	Widths of iron ribs, mm
ED	Electrical degree
MD	Mechanical degree
g	Air-gap length, mm
h_{as}	Height of air-space flux barrier, mm
H_{ci}	Coercivity of PMs, MA/m
I_s	Amplitude of stator phase current, A
L_{st}	Active axial length, mm
N_s	Number of stator slots
N_c	Number of turns per slot
p	Number of pole pairs
P_{cu}	Copper loss, W
P_{iron}	Iron loss, W
P_{eddy}, P_{hys}	Eddy current iron loss and hysteresis iron loss, W
R_{rin}, R_{rout}	Rotor inner and outer radii, mm
R_{sout}	Stator outer radius, mm
T_{syn}^A	Average (synthetic) torque amplitude, Nm
T_m^A	PM torque amplitude, Nm
T_r^A	Reluctance torque amplitude, Nm
THD	Total harmonic distortion, %
V_{mag}	Volume of permanent magnets, mm³
w_l, h_l	Width and height of large PM, mm
w_r, h_r	Width and height of small PM, mm
w_s, h_s	Stator tooth width and stator slot height, Mm
β	Current advancing angle of stator winding, ED
$\triangle\beta$	Current angle difference between maximum PM and reluctance torque components, ED
θ	Spatial angle, ED
θ_{ap}	Pole arc of whole cavity between left and right rotor cavities in each pole, ED
$\theta_{lap}, \theta_{rap}$	Arc pitch between rotor cavities, ED
θ_{rn}, d_{rn}	Rotor notch position, ED, and notch depth, mm

I. INTRODUCTION

ELECTRIC vehicles (EVs) have become increasingly attractive recently due to the rapid development of intelligential control technology and concerns about fossil fuel. Developing advanced electrical machines with high performance including torque density, constant power speed range (CPSR), efficiency and reliability etc. has attracted great interests by both academia and industry because they are one of the primary components of electric propulsion system in EVs. Up to now, various machine topologies have been proposed for EV application, including electrically excited synchronous machines, induction

machines, permanent magnet (PM) machines [1]–[3] and some novel machines such as magnetic modulation PM machines, switched flux PM machines and memory PM machines [4]–[6]. Although different topologies show their specific advantages, interior permanent magnet (IPM) machines remain the most widely employed due to superior torque density, high efficiency, wide CPSR, mechanical robustness especially for high-speed operation conditions, and easy manufacturing [7]–[10].

To achieve high torque density of the IPM machines, many studies have been reported. According to the torque production of IPMs, three technical concepts can be employed for torque enhancement:

- Increasing the amplitude of PM torque T_m^A;
- Increasing the amplitude of reluctance torque T_r^A;
- Reducing the current advancing angle difference between maximum PM and reluctance torque components $\triangle\beta$.

The increase of T_m^A can be easily achieved by more PM usage or using PM material with better characteristics. However, it is not only costly but also rising concerns for resource crisis due to unsustainable rare earth PM material. IPMs employing the second approach, i.e., utilizing high proportion of reluctance torque, is often used to reduce the usage of PMs, which are designated as PM-assisted synchronous reluctance machines (PMASRMs) in literature [11]–[13]. Nevertheless, PMASRMs usually exhibit complicated rotor geometry: many pieces of PMs and multi-layer rotor structures, resulting in drawbacks in mechanical strength and high manufacturing costs.

The concept of reducing $\triangle\beta$ provides a new approach for torque enhancement and is designated as the magnetic-field shifting (MFS) effect in this paper. This concept aims to shift the axes of PM field and reluctances, thereby adjusting the current advancing angles of peak PM and reluctance torque components to reduce the current angle difference between them. Consequently, the current advancing angles for maximum PM and reluctance torque components become closer and the maximum average torque is enhanced without the increase of PM usage. Thus, higher torque density can be achieved and both PM and reluctance torque components are better utilized at the maximum synthetic torque condition.

To utilize the MFS effect, specific machine designs are required that are typically asymmetric rotor designs. Several relevant studies have already been reported in [14]–[25]. In [14] and [15], extra interior barriers are equipped to employ MFS effect. For inset IPM designs, MFS effect can be achieved by the axis shifting of inset PMs in [16] and [17]. More specifically, a hybrid rotor configuration that exhibits a pole with inset interior PM and a pole with V-shape interior PMs alternatively is investigated in [18], [19]. Asymmetric IPMs with symmetrical cavity structures and asymmetric PM configurations are proposed in [20] and [21], which can make the optimal current angles for the peak points of two torque components to be approximately equal. [22] proposes an AIPM topology for hybrid EV that has a flux barrier between two PMs of a skewed V-shape IPM as magnetic slits in each pole for asymmetric field construction. The AIPM proposed in [22] is compared with conventional V- and bar-sharp IPMs in [23] all with the same fractional slot concentrated winding stator, which shows that the AIPM design has negligible torque enhancement compared with the

V-shape IPM and the bar-shape topology has the highest torque. However, the AIPM design in [23] aims to improve the torque performance by reducing the cross-magnetization effect, as its small reluctance torque compared with PM torque diminishes the possibility of utilizing MFS effect for torque enhancement. Axial asymmetric structures have been reported in [24] and [25]. In [24], a surface-mounted PM (SPM) rotor and a reluctance rotor are axially connected, which make it easy to adjust the adjacent angle between the axes of both rotors. [25] proposes an axially sandwiched topology with an SPM rotor connecting with two reluctance rotors at both sides. These topologies show good performance but are mechanically complex. Except for torque enhancement, asymmetric rotor designs are also employed for torque ripple and vibration reduction in [26] and [27], respectively.

Although some inspirable work has been reported in the reviewed literature, complicated rotor structure remains a concern for asymmetric topologies. In this paper, a novel asymmetric interior permanent magnet (AIPM) synchronous machine is proposed for EVs that exhibits relatively simple structure with skewed V-shape PMs and flux barriers. The most distinguished feature of the proposed AIPM machine is that it has a flux barrier outside the skewed V-shape PM rotor, rather than a flux barrier inside the skewed V-shape PM rotor as in [22]. The paper is organized as follows. Section II describes the proposed AIPM topology, together with an existing AIPM topology proposed in [22] that also uses skewed V-shape PM configuration and the conventional V-shape IPM benchmark employed as Toyota Prius 2010 MG2 [28]. The two AIPMs are designed with the same stator, rotor diameter and total PM volume as the IPM benchmark. Section III investigates the influences of PM cavity and flux barrier positions in both AIPMs on maximum synthetic torque, and their optimal designs are obtained by considering mechanical strength of rotor designs. In Section IV, electromagnetic and steady-state thermal performances of three machines are compared to verify the merits of the proposed AIPM topology. The experimental results of the small-scale prototype are given in Section V to validate the concept of proposed AIPM machine, followed by the conclusion in Section VI.

II. MACHINE TOPOLOGIES

Cross sections of three topologies, namely the proposed AIPM, the existing AIPM proposed by Mitsubishi in [22] and the conventional IPM benchmark of Prius 2010 [28] are illustrated in Fig. 1, where the arrows in PMs denote the magnetization direction. The proposed AIPM is featured by skewed V-shape PMs using two PMs in each pole with different dimensions and an additional flux barrier outside the PM cavity in each pole. More specifically, the flux barriers of AIPM-I are located between V-shape PMs of adjacent poles, whose inner end is located near the bottom of the V-shape cavity and the outer end is located near the rotor surface. For comparison, the existing AIPM-II [22] also has skewed V-shape PMs but the flux barriers are located inside the V-shape PMs between the PM cavity and the rotor surface. In both AIPM topologies, two PMs with different dimensions are employed not only due to geometric restriction but also for effective allocation of PMs. Moreover, both AIPMs have similar
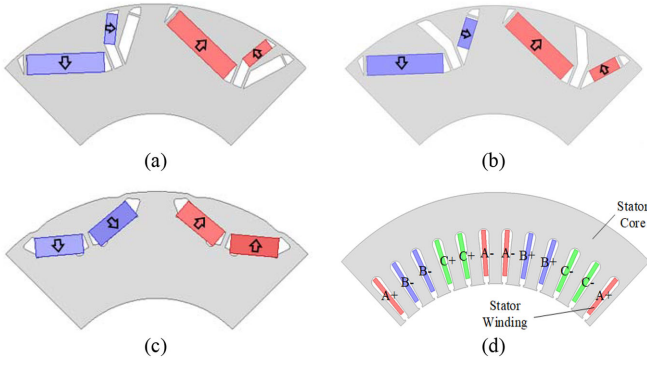
Fig. 1. Cross sections of topologies. (a) Proposed AIPM-I, (b) Existing AIPM-II [22], (c) IPM benchmark (Toyota Prius 2010), (d) Shared stator (Toyota Prius-2010).

Fig. 3. Influences of θ_{lap} on maximum torque of AIPMs at 750 r/min, 236 A current amplitude and $\theta_{ap} = 132$ ED.

design are removed and rotor inner diameter is correspondingly modified.

Based on Fig. 2, for both AIPMs, the positions of outer ends of PM cavities and the flux barrier near the rotor surface, together with pole arcs and arc pitches, should meet the following formulas to achieve asymmetric PM field distribution.

$$\begin{cases} \theta_{ap} = \theta_{lap} + \theta_{rap} \\ \theta_{lap} > \theta_{ap}/2 > \theta_{rap} \\ \theta_{ap} < \pi \end{cases} \tag{1}$$

The relationships between thicknesses of PM cavities and airspace flux barrier in AIPM machines and between PM widths in AIPMs should meet (2) and (3), respectively.

$$h_l < h_r + h_{as} \tag{2}$$

$$w_l > w_r \tag{3}$$

III. INFLUENCES OF CAVITY POSITIONS ON MAXIMUM AVERAGE TORQUE AND OPTIMAL DESIGNS

As illustrated in Fig. 1, rotor structures of both AIPM machines are featured by three cavities whose outer ends are located near the rotor surface separately while their inner ends are located closely. The outer end positions of cavities, as shown in Fig. 2, act as key rotor geometric parameters of AIPMs. In this section, the influences of outer end positions of cavities on maximum torque are investigated at 750 r/min and 236 A under maximum torque per ampere (MTPA) control [28] that is a typical condition for maximum torque in the constant-torque region.

A. Influence of Position of Top Cavity

The outer end positions of top cavities in both AIPM machines are characterized by θ_{lap}. The influences of θ_{lap} on maximum average torque in both machines with constant θ_{ap} are shown in Fig. 3. The optimal θ_{lap} of AIPM-I for maximum torque exists at 104 ED when the top cavity is closer to the right cavity than the left cavity. The waveform of AIPM-II shows two peaks at a small and a large θ_{lap} when the top cavity is located close to the left and right cavity, respectively, but the maximum torque point is found when the outer end of the top cavity is much closer to the right cavity. In general, the maximum torque of AIPM-I is larger than that of AIPM-II, while the influence of θ_{la_p} on
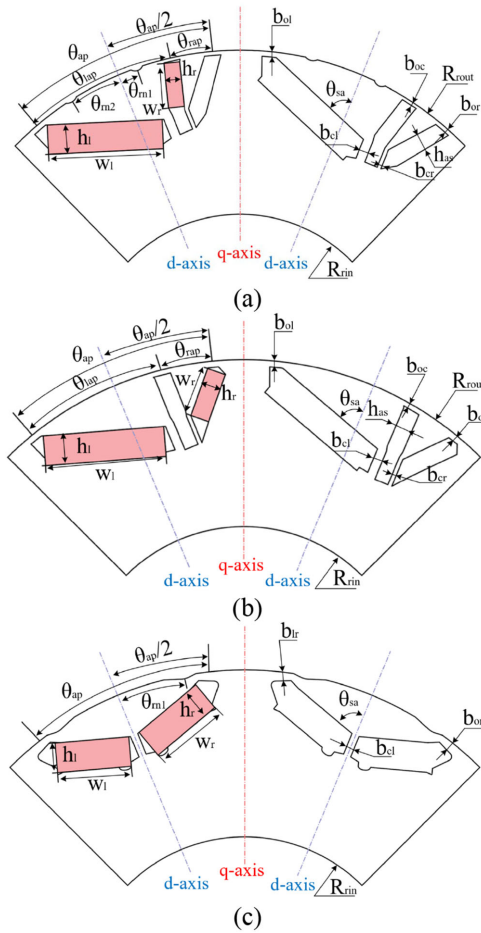

Fig. 2. Key rotor geometric parameters of three machines. (a) AIPM-I, (b) AIPM-II, (c) IPM.

rotor cavity structure although locations of the small PM and of the flux barrier are different. The rotor structures and key geometric parameters of three machines are shown in Fig. 2. The 48-slot/8-pole IPM design of Prius 2010 MG2 with distributed windings is employed as the benchmark as shown in Fig. 1(c). Both AIPM-I and AIPM-II are designed using the same stator, rotor diameter, axial length and total PM volume to perform a fair comparison. For simplification, rotor air holes of the initial
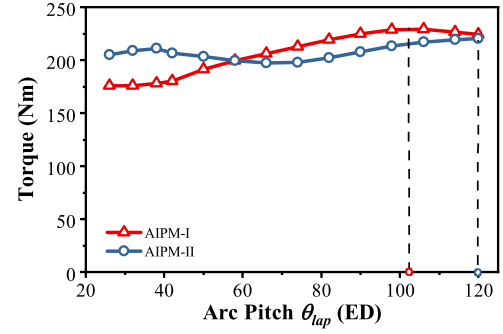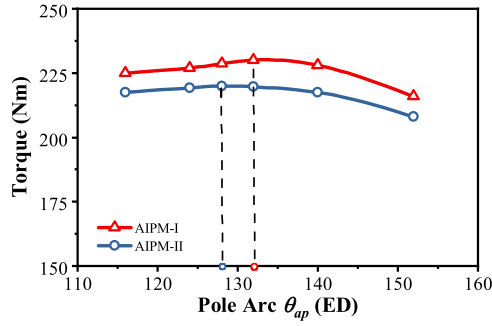
Fig. 4. Influences of θ_{ap} on maximum torque of AIPMs at 750 r/min, 236 A current amplitude and θ_{lap} optimized for maximum torque in each case.
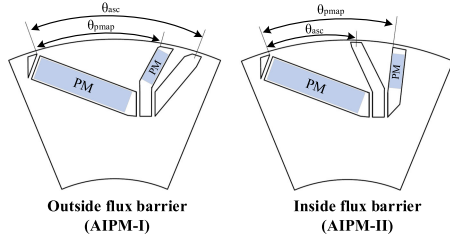

Fig. 5. Geometric structure comparison between AIPM-I and AIPM-II in the aspect of the flux barrier position.

maximum torque in AIPM-I is also relatively more significant than that in AIPM-II.

B. Influence of Pole Arc

The influences of the pole arc θ_{ap} of the whole cavity in each pole of both AIPMs on maximum torque are investigated in Fig. 5. With the variation of pole arc θ_{ap}, the outer end position of the top cavity is optimized for maximum torque in each case. As shown in Fig. 4, the optimal parameters of both asymmetric topologies exist and the maximum torque of AIPM-I remains larger than that of AIPM-II.

C. Influence of Position of Flux Barrier

As illustrated in Fig. 5, the difference between geometric structure of AIPM-I and AIPM-II can be regarded as whether the flux barrier is located outside the skewed V-shape cavity (AIPM-I) or is located inside the cavity (AIPM-II). To reveal the mechanism of flux barrier position for maximum torque enhancement, the models of both AIPMs are unified with the same pole arc of PMs that is featured by θ_{pmap} in Fig. 5, while the position of the flux barrier is featured by θ_{asc}. The effect of θ_{asc} with both inside and outside flux barrier designs on maximum average torque is shown in Fig. 6. AIPM-I has higher maximum torque than the optimal design of AIPM-II, while the optimal position of the flux barrier in AIPM-II for maximum torque is achieved when the flux barrier is located significantly close to the right-side PM cavity. It has revealed that the maximum torques of outside flux barrier designs are generally larger than the maximum torque of the inside flux barrier model. It can also explain why the optimal θ_{lap} of AIPM-II is located at the maximum θ_{lap} design, because the maximum average torque
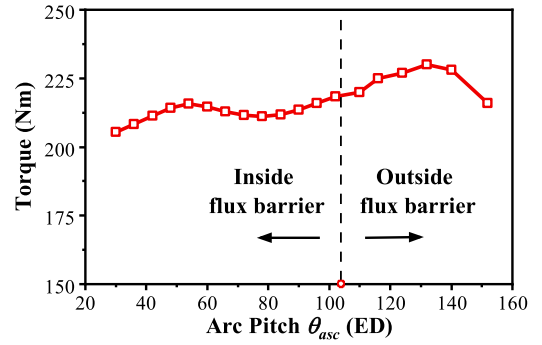

Fig. 6. Influence of flux barrier position θ_{asc} on maximum torque in AIPMs at 750 r/min, 236 A current amplitude and θ_{pmap} at 104 ED.
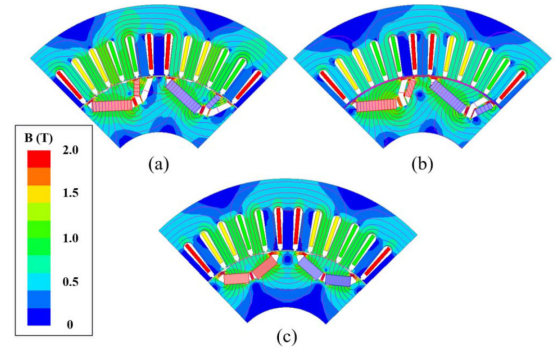

Fig. 7. Optimal designs and open-circuit magnetic field and flux line distributions of AIPMs. (a) AIPM-I, (b) AIPM-II, (c) IPM.

can be further promoted when shifting the flux barrier out of the skewed V-shape PM cavity.

D. Design Optimization of AIPMs

Based on the previous investigations, the two AIPMs are optimized for maximizing average torque with the same stator, rotor diameter, axial length and total PM volume as the IPM benchmark. Besides, von-Mises mechanical stress and torque ripple are also considered for design optimization of two AIPMs. Maximum average torque and torque ripple are obtained at 750 r/min, 236 A under MTPA control, and maximum von-Mises stresses are calculated at 14000 r/min. Torque ripples of optimal AIPM designs are required to be smaller than that of the IPM benchmark (Prius 2010), while maximum von-Mises stresses in AIPMs should be similar as that in the IPM. To reduce the torque ripple of AIPM-I, the rotor surface shaping technique [29] similar to Prius 2010 is employed. The optimal designs of AIPMs and their open-circuit magnetic field and flux line distributions are shown in Fig. 7. The von-Mises stress distributions in rotor cores of two optimal AIPM machines and the IPM benchmark at 14000 r/min are compared in Fig. 8. It confirms that maximum stresses of two optimal AIPM designs are similar to that in IPM and maximum stress regions are all located in the iron ribs between cavities. The key design parameters of two AIPM topologies and the IPM benchmark are shown in Table I. It should be noted that the relatively small B_{res} is due to the influence of temperature rise at high load condition with 236 A current amplitude that is provided in [28].
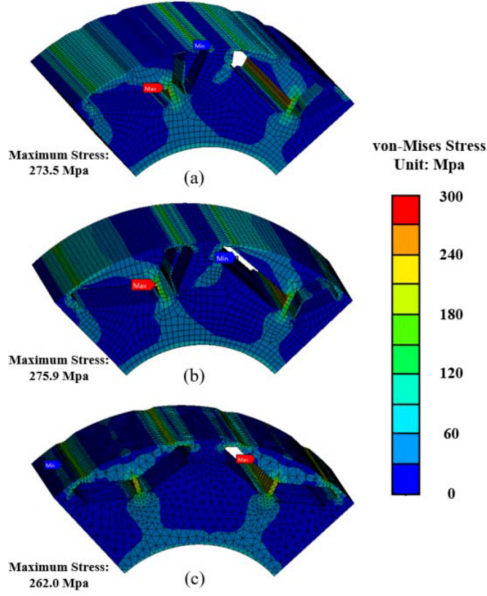
Fig. 8. Von-Mises stress distributions in rotor cores at 14000 r/min. (a) AIPM-I, (b) AIPM-II, (c) IPM.

TABLE I
KEY DESIGN PARAMETERS OF AIPM TOPOLOGIES

Parameters	Unit	AIPM-I	AIPM-II	IPM
N_s	-	48	48	48
N_c	-	11	11	11
R_{sout}	mm	132	132	132
h_s	mm	31	31	31
w_s	mm	7.3	7.3	7.3
Winding type	-	Single-layer short-pitch winding		
p	-	4	4	4
g	mm	0.82	0.82	0.82
L_{st}	mm	50.8	50.8	50.8
R_{rin}	mm	45	45	45
R_{rout}	mm	80.22	80.22	80.22
V_{mag}	mm³	104460	104460	104460
B_{res}	T	1.051	1.051	1.051
H_{ci}	MA/m	1.03	1.03	1.03
μ_r	-	1.05	1.05	1.05
θ_{ap}	ED	140	138	128
θ_{lap}	ED	108	121	-
θ_{as}	MD	70	74	72
h_l	mm	7.2	7.2	7.2
w_l	mm	28.3	28.3	17.88
h_r	mm	4.5	4.5	7.2
w_r	mm	12	12	17.88
h_{as}	mm	4	4	-
b_{cl}	mm	2.5	2.3	1.9
b_{cr}	mm	1.0	1.0	-
b_{ol}	mm	1.8	1.7	2.2
b_{or}	mm	1.2	1.5	2.2
b_{oc}	mm	1.5	1.1	-
$\theta_{rn1}, \theta_{rn2}$	ED	18.6, 25.1	-	45.6, 45.6
d_{rn1}, d_{rn2}	mm	0.84, 0.92	-	0.85, 0.85

IV. MACHINE PERFORMANCE COMPARISON

To reveal the merits and demerits of the proposed AIPM and to confirm the mechanism of torque enhancement in AIPMs, electromagnetic performances of two AIPMs and the IPM benchmark are compared in this section, while steady-state thermal analyses are also performed.
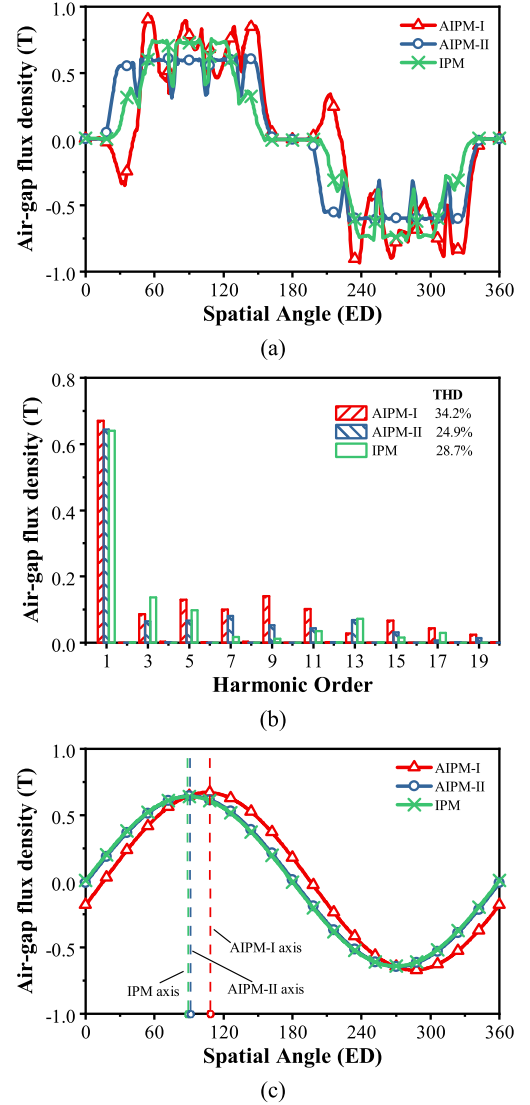

Fig. 9. Open-circuit air-gap flux densities. (a) Waveforms, (b) Spectra, (c) Waveforms of fundamental components.

A. Open-Circuit Performances

The open-circuit air-gap flux density waveforms and their spectra are compared in Fig. 9. Compared with other machines, the proposed AIPM-I has the highest amplitude and the most serious harmonic distortion denoted by the highest THD value. As to the existing AIPM-II, it has slightly smaller distortion of waveform, similar amplitude of fundamental flux density and smaller THD than the IPM. The fundamental components of three machines are extracted as shown in Fig. 9(c). AIPM-I shows clear axis-shifting of the waveform compared with that of IPM, while the axis-shifting of AIPM-II is negligible, which indicates significant MFS effect in AIPM-I but negligible MFS effect in AIPM-II.

Fig. 10 shows the back electromotive forces (EMFs) of three machines. Similar with the open-circuit air-gap flux density, AIPM-I has the highest fundamental back EMF and the highest THD, while IPM shows the smallest fundamental back EMF and
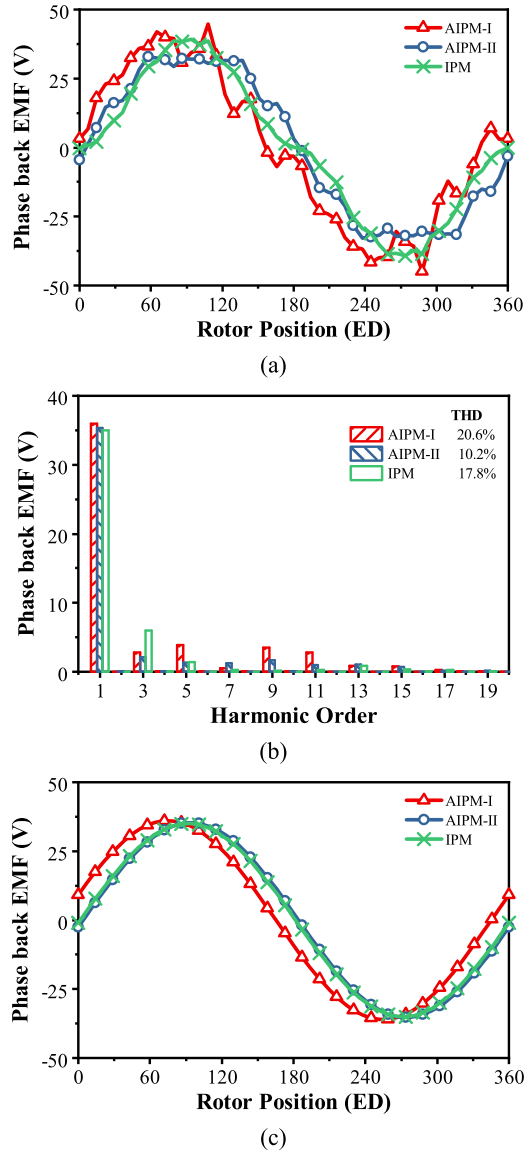
Fig. 10. Open-circuit phase back EMFs at 750 r/min. (a) Waveforms, (b) Spectra, (c) Waveforms of fundamental components.

TABLE II
COMPARISON OF SALIENCY RATIOS

Performance	AIPM-I	AIPM-II	IPM
L_d (mH)	2.3	2.7	2.6
L_q (mH)	5.1	6.0	5.8
L_q- L_d (mH)	2.9	3.3	3.2
Saliency ratio L_q/L_d	2.217	2.222	2.231

*Performances are evaluated with only PM excitation. L_d and L_q are *d*- and *q*-axis inductances.

AIPM-II has the smallest THD of back EMF waveform. Clear axis-shifting can also be observed in the fundamental back EMF waveform of AIPM-I compared with that of other machines as shown in Fig. 10(c).

The saliency ratios of three machines at the condition with only PM excitation, according to the *d-q* frame defined in Fig. 2,
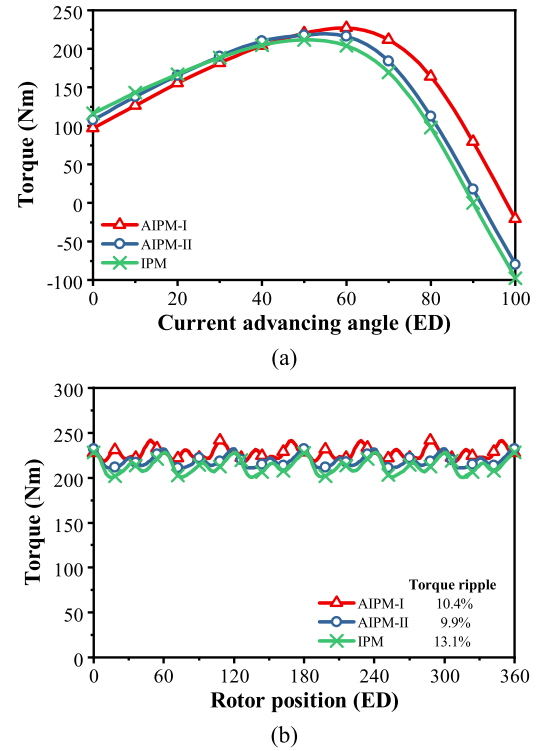

Fig. 11. Torque performance comparison at 750 r/min and 236 A. (a) Average torques vs current advancing angles, (b) Torque waveforms at maximum torque condition.

are shown in Table II. In general, the saliency ratios of the three machines are similar.

B. Torque Performance

The average torque-current advancing angle performances of three machines at 750 r/min and 236 A are compared in Fig. 11(a) and their torque waveforms at the maximum torque conditions under MTPA control are shown in Fig. 11(b). AIPM-I has the highest average torque in three machines with the same PM usage, while AIPM-II also shows clear torque enhancement compared with the IPM benchmark. Besides, evident shifting of maximum torque points in torque-current angle performances can be observed in AIPM-I. By comparing waveforms of AIPM-I and IPM, it is found that the current angles for maximum average torque and for zero average torque of AIPM-I are clearly larger than those of the IPM benchmark. As shown in Fig. 11(b), torque ripple ratios of three machines are similar at their maximum torque conditions according to the design optimization goals of AIPMs. In detail, the AIPM-II has the smallest torque ripple, followed by AIPM-I, while the torque ripple of the IPM benchmark is slightly higher than that of both AIPMs. The maximum average torques and torque ripples of three machines at these conditions are also shown in Table III. It shows that AIPM-I has smaller torque ripple than the IPM benchmark with and without rotor notches, respectively. The significant effect of rotor notches in reducing torque ripple in AIPM-I and IPM are also confirmed.

To reveal the mechanism of torque enhancement, torque components of three topologies are extracted as PM and reluctance

Perfor mance	AIPM-I		AIPM-II	IPM	
	With notches	Without notches	With notches	With notches	Without notches
$T_{syn}{}^A$	228.4	232.6	218.5	211.6	214.8
$T_{p\text{-}p}$	10.4%	18.8%	9.9%	13.1%	21.7%

*Performances are evaluated at 750 r/min and 236 A current amplitude at maximum torque conditions under MTPA control for each design.
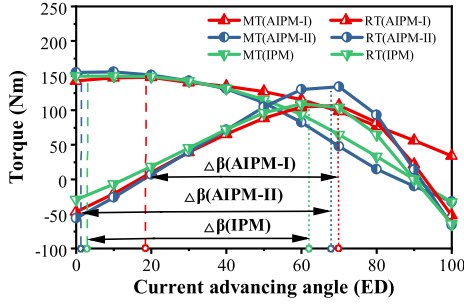

Fig. 12. Extraction of torque components of three topologies at 750 r/min and 236 A.

TABLE IV
KEY TORQUE PERFORMANCE OF THREE TOPOLOGIES

Performance	AIPM-I	AIPM-II	IPM
$T_{syn}{}^A$	228.4	218.5	211.6
$T_m{}^A$	148	155	150
$T_r{}^A$	106	135	113
$\triangle\beta$	48	67	60
TE	8.0%	3.3%	---

*Performances are evaluated at 750 r/min and 236 A, TE is the torque enhancement ratio of topologies comparing with the IPM.

torque components by using frozen permeability method (FPM) [30]. The PM and reluctance torque components at 750 r/min and 236 A current amplitude are shown in Fig. 12, where MT and RT denote PM and reluctance torque components, respectively.

As shown in Fig. 12, the maximum PM torque components of three machines are similar although the proposed AIPM-I produces slightly smaller value than other two machines. AIPM-II has the largest maximum reluctance torque, followed by IPM, and the proposed AIPM-I has the smallest value. Besides, a significant reduction of angle difference $\triangle\beta$ in AIPM-I between maximum PM and reluctance torque components can be clearly observed, compared with the existing AIPM-II and the IPM benchmark. Key torque performances are also compared in Table IV, which confirms that the significant torque enhancement of the proposed AIPM-I is achieved by MFS effect as the $\triangle\beta$ of AIPM-I is about 12 ED smaller than IPM. However, it is also found that the $\triangle\beta$ of AIPM-II is even larger than the IPM benchmark, which denotes a negative MFS effect. Therefore, the small torque enhancement of AIPM-II is mainly due to its high amplitudes of both PM and reluctance torque components, rather than employing MFS effect.

The influences of armature reaction on maximum average torque of three machines obtained by MTPA are compared in Fig. 13. It confirms that the proposed AIPM-I remains the
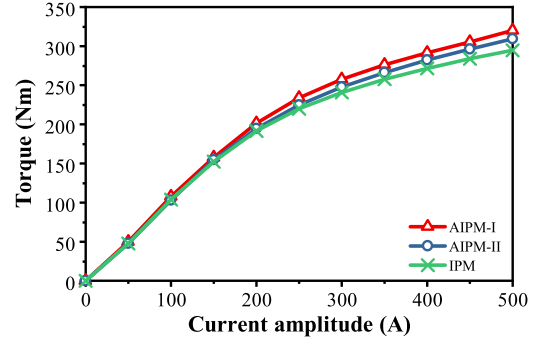

Fig. 13. Variation of average torques at 750 r/min with current amplitude using MTPA.
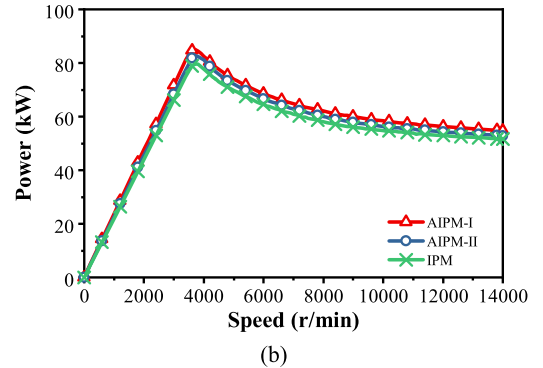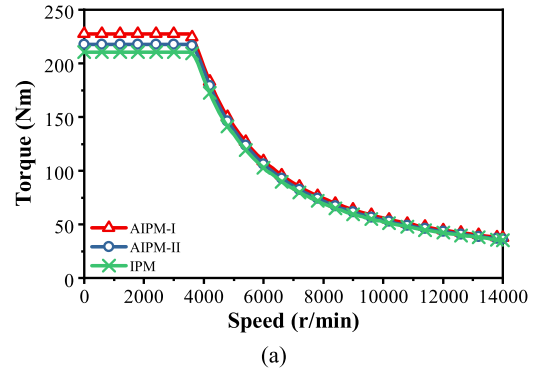

(a)

(b)

Fig. 14. Torque and power-speed curves. (a) Torque-speed curve, (b) Power-speed curve.

merit for torque enhancement across the whole span of current amplitude, compared with AIPM-II and the IPM benchmark.

C. Torque/Power-Speed Envelops

Wide CPSR is an essential requirement for IPMs in EVs. The torque- and power-speed curves of three machines are evaluated and compared based on the computation method proposed in [31], as shown in Fig. 14. In the calculation, the constraints of DC voltage and maximum current amplitude are 650 V and 236 A, respectively.

Fig. 14 indicates that all the three machines can reach wide speed range up to 14000 r/min. The proposed AIPM-I remains the highest torque and power across the speed range compared with its counterparts. AIPM-II also shows higher torque and power in both the constant-torque region and the constant-power region than the IPM benchmark.
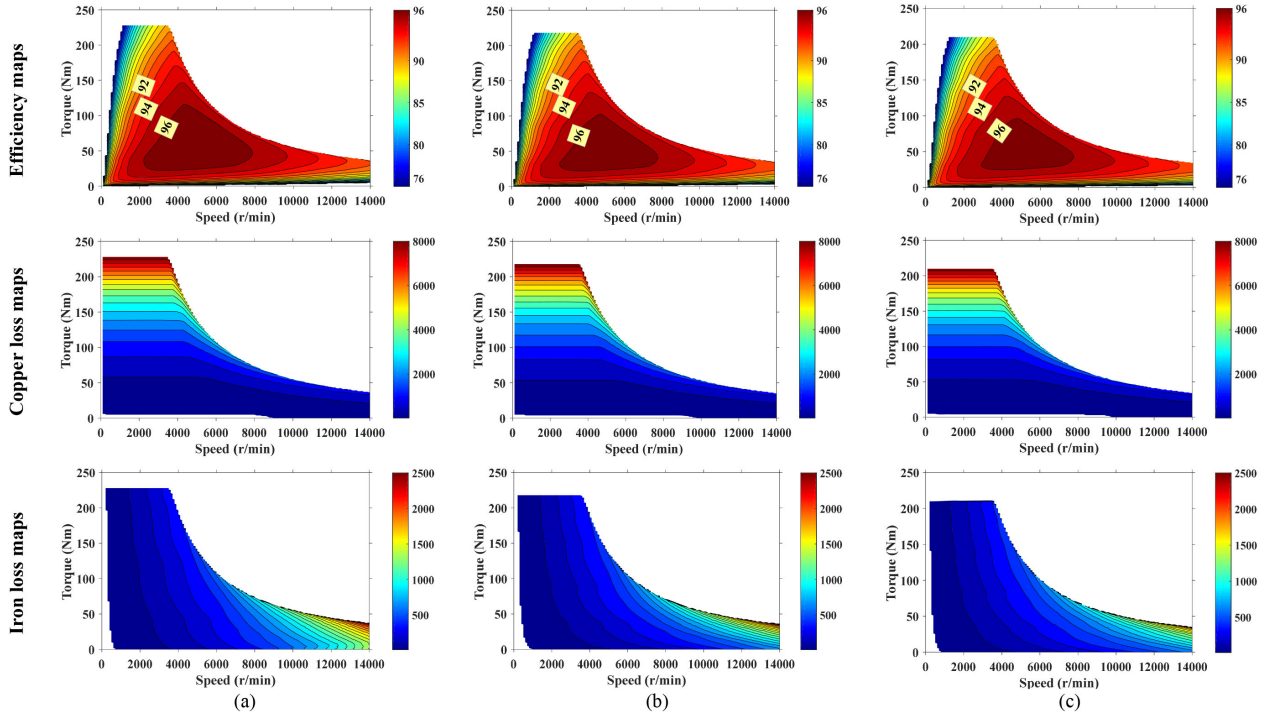
Fig. 15. Efficiency, copper loss, and iron loss maps. (a) AIPM-I, (b) AIPM-II, (c) IPM.

D. Efficiency and Loss Maps

The Efficiency and Loss Maps are Calculated By FE Analysis Using the Method Reported in [31]. The copper Loss Is Calculated By

$$P_{cu} = 1.5 R_0 I_s^2 \qquad (4)$$

where R_0 is the phase winding resistance.

The iron loss is obtained as the sum of two iron loss components: hysteresis iron loss and eddy current iron loss that are calculated directly by FE analysis:

$$P_{iron} = P_{hys}(I_s, \beta, n_r) + P_{eddy}(I_s, \beta, n_r) \qquad (5)$$

where n_r is the rotor speed.

The efficiency, copper loss and iron loss maps for the three machines under 650 V DC voltage and 236 A are compared in Fig. 15. In Fig. 15(a), only regions with efficiency higher than 75% are presented. The proposed AIPM-I has high efficiency in the low-speed region and the largest high efficiency region ($\geq$96%), compared with AIPM-II and IPM. However, when the speed is higher than 12000 r/min, AIPM-I shows lower efficiency than other two machines.

The efficiency increase of AIPM-I at low-speed can be explained by the copper and iron loss maps. As shown in Fig. 16, copper loss is generally the dominant loss when the speed is lower than 10000 r/min and the torque enhancement in AIPM-I clearly reduces the required stator current to generate the required output torque compared with AIPM-II and the IPM. Thus, the copper loss in AIPM-I decreases and the efficiency improves.

However, as also indicated in iron loss maps in Fig. 15, iron losses of all three machines are mainly affected by the speed.
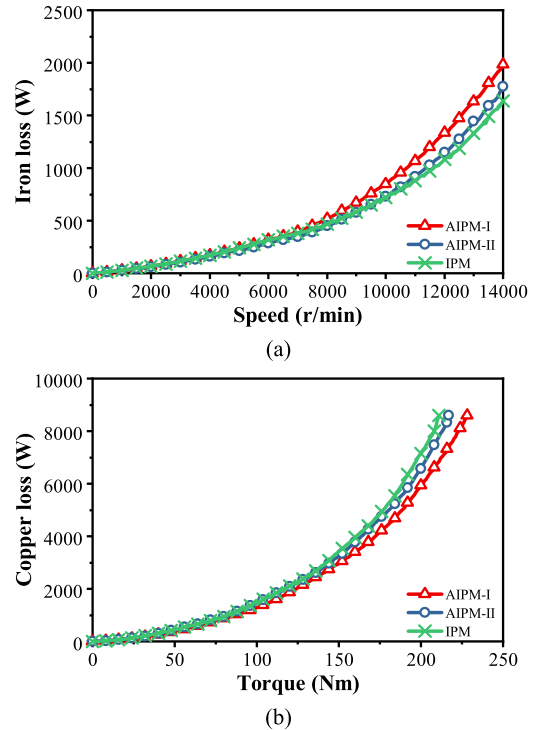

Fig. 16. Loss comparison of three machines. (a) Iron loss versus speed at 30 Nm torque, (b) Copper loss versus torque at 750 r/min.

The iron loss of AIPM-I at high speed range ($\geq$10000 r/min) is significantly higher than those of both AIPM-II and IPM, mainly due to its highest harmonic distortion in the open-circuit magnetic flux density waveform. Therefore, at high speed when iron
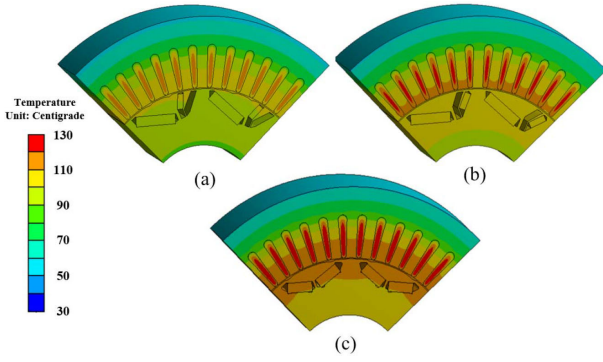
Fig. 17.   Temperature distributions of three machines at 150 Nm and 750 r/min. (a) AIPM-I, (b) AIPM-II, (c) IPM.

loss becomes dominant, the proposed AIPM-I shows slightly lower efficiency than AIPM-II and Prius 2010 IPM.

For more detailed comparison, the iron losses of three machines at the same torque across the whole speed range are compared in Fig. 16(a). AIPM-I shows the highest iron loss across the whole speed range but the difference only becomes obvious at high speed. The iron loss of AIPM-II is slightly smaller than that of IPM at low-speed, but this merit diminishes with the increase of speed and AIPM-II shows even higher iron loss compared with the IPM when speed is higher than 12000 r/min. Fig. 16(b) shows that the copper losses of three machines increase with the output torque. It also indicates that the copper loss in AIPM-I is significantly lower at high output torque compared with the Prius 2010 IPM for the same torque.

E. Steady-State Thermal Analysis

To compare the steady-state temperature rises of three machines at different torque and speed, the steady-state thermal analysis has been carried out. As structure and parameters of coolant design in Prius 2010 has not been reported in detail in [28], the thermal conductivity characteristics of materials and heat convention coefficients are mostly obtained according to methods provided in [32] and [33], while the ambient temperature on stator surface as an equivalence of the coolant are set as 25 [28] for the three machines to perform the comparison. The temperature distributions of three topologies at 150 Nm and 750 r/min are compared in Fig. 17.

In Fig. 18(a), the temperature rises of the three machines at different torque but the same speed 750 r/min are compared. It shows AIPM has the smallest temperature due to torque enhancement and corresponding reduction of copper loss. The variations of temperature versus speed at 50 Nm in the three machines are compared in Fig. 18(b). AIPM-I has the lowest temperature rises in winding, core and PM at low-speed conditions but its temperature rise becomes the highest at high speed (11000 r/min) due to high iron loss, which is consistent with the loss analysis in Section IV.D. It should be noted that steady-state temperatures under conditions of high torque larger than 150 Nm or high speed are calculated only for reference as these conditions are not designed for continuing operation in the Prius 2010 IPM.
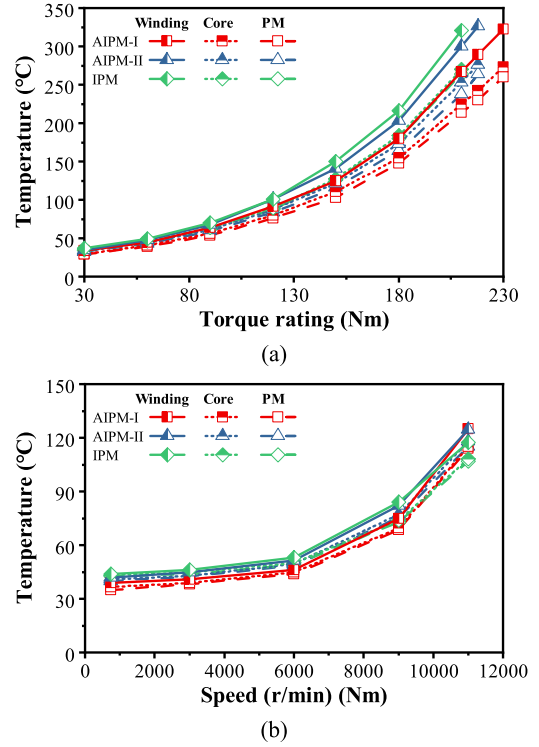

Fig. 18.   Temperature comparison of three machines. (a) Different output torque at 750 r/min, (b) Different speed at 50 Nm.

TABLE V
KEY DESIGN PARAMETERS OF SMALL-SCALE AIPM-I PROTOTYPE

Parameter	Unit	Value
N_s	-	24
p	-	2
g	mm	1.0
L_{st}	mm	50.0
R_{rout}	mm	24.0
V_{mag}	mm^3	12600
B_{res}	T	1.23
θ_{ap}	ED	132
θ_{lap}	ED	106
h_l	mm	3.5
h_r	mm	2.0
b_{ol}, b_{or}	mm	0.5

V. EXPERIMENTAL VALIDATION

In order to verify the accuracy of FE calculation and the concept of the proposed AIPM-I topology, a small-scale prototype of the proposed AIPM-I machine is designed, manufactured and tested due to cost and experiment platform limits. The small-scale 24-slot/4-pole AIPM-I machine has distributed windings and a 100mm stator outer diameter. The basic parameters of prototype design are shown in Table V and pictures of the prototype, including laminations, stator and rotor, are illustrated in Fig. 19. The picture of the test bench is shown in Fig. 20.

The line back-EMF waveforms and spectra of FE-predicted and measured results at 1500 r/min at open-circuit condition are compared in Fig. 21. The test results of static torque performance at different current amplitudes are compared with FE analyses in Fig. 22.
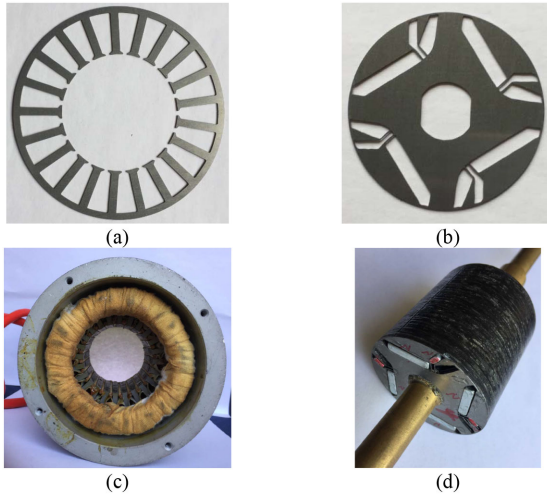
Fig. 19. Pictures of the prototype AIPM-I. (a) Stator lamination, (b) Rotor lamination, (c) Stator, (d) Rotor.
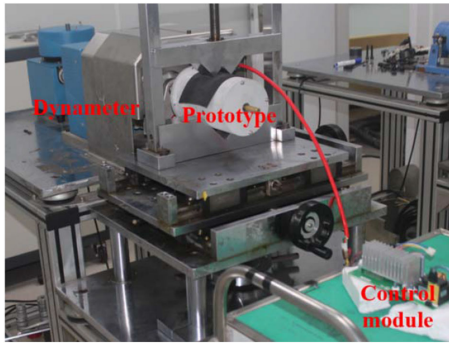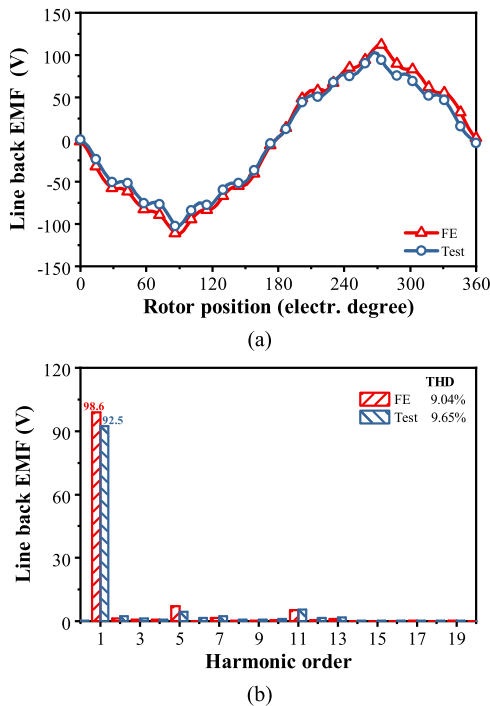

Fig. 20. Test bench.

Fig. 21. Comparison between FE predicted and measured line back-EMF waveforms at 1500 r/min. (a) Waveforms, (b) Spectra.
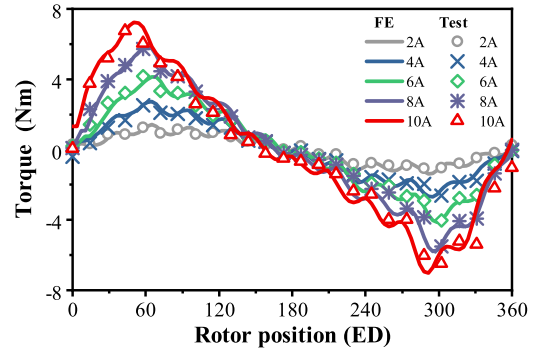

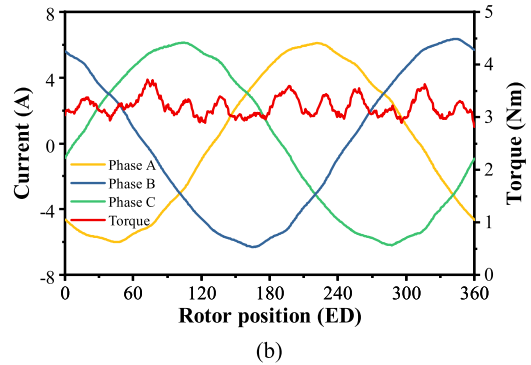Fig. 22. Static torque performance comparison between FE and test.
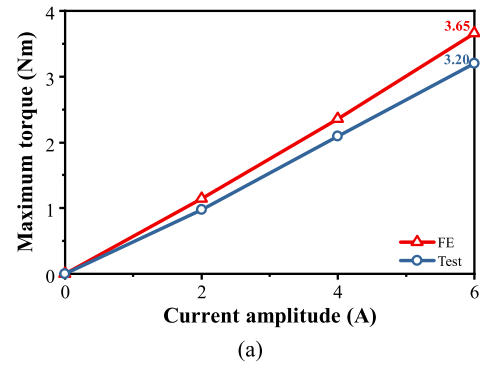
Fig. 23. Dynamic measured results at 1500 r/min. (a) Variation of FE and measured maximum average torque with current, (b) Measured results of current and torque waveforms at 6 A under MTPA control.

The FE and measured results of maximum average torque are compared in Fig. 23(a). The experimental results are obtained by dynamic tests at 1500 r/min. The errors between FE and measured results of back EMF and maximum average torque at 6 A for the small-scale prototype are 6.2% and 12.3%, respectively. Fig. 23(b) illustrates the waveforms of three-phase currents and torque at 6 A.

VI. CONCLUSION

In this paper, a novel AIPM topology featured by skewed V-shape PMs and an extra flux barrier outside the PM cavity in each pole for torque enhancement by utilizing MFS effect is proposed for EV application. The proposed topology shows significant MFS effect and torque enhancement, and benefits

from simple structure with single layer PM configuration and only two pieces of PMs per pole.

The proposed AIPM-I and existing AIPM-II machines are designed with the same stator, rotor diameter and PM usage and can achieve similar mechanical strength as the IPM benchmark (Prius 2010). The proposed AIPM-I shows significant torque enhancement compared with the existing AIPM-II and the IPM benchmark and confirms that the increase of maximum torque is achieved by utilizing MFS effect. It shows that the outside flux barrier design of the proposed AIPM-I can inherently produce higher average torque than the inside flux barrier design of the existing AIPM-II. The proposed AIPM machine also has wide CPSR, small torque ripple and high efficiency especially in the low-speed region, while shows demerits including high open-circuit harmonic distortion and low efficiency in the high-speed region which needs to be solved in the future research. It proves that the proposed AIPM-I is a competitive machine topology for EVs. The accuracy of FE results is validated by experimental results of the small-scale prototype.

REFERENCES

[1] Z. Zhu and D. Howe, "Electrical machines and drives for electric, hybrid, and fuel cell vehicles," *Proc. IEEE*, vol. 95, no. 4, pp. 746–765, Apr. 2007.

[2] Z. Zhu, W. Chu, and Y. Guan, "Quantitative comparison of electromagnetic performance of electrical machines for HEVs/EVs," *CES Trans. Elect. Mach. Syst.*, vol. 1, no. 1, pp. 37–47, Jul. 2017.

[3] K. T. Chau, C. C. Chan, and C. Liu, "Overview of permanent-magnet brushless drives for electric and hybrid electric vehicles," *IEEE Trans. Ind. Electron.*, vol. 55, no. 6, pp. 2246–2257, May 2008.

[4] I. Boldea, L. N. Tutelea, L. Parsa, and D. Dorrell, "Automotive electric propulsion systems with reduced or no permanent magnets: An overview," *IEEE Trans. Ind. Electron.*, vol. 61, no. 10, pp. 5696–5711, Jan. 2014.

[5] H. Yang, H. Lin, Z. Zhu, D. Wang, S. Fang, and Y. Huang, "A variable-flux hybrid-PM switched-flux memory machine for EV/HEV applications," *IEEE Trans. Ind. Appl.*, vol. 52, no. 3, pp. 2203–2214, Feb. 2016.

[6] M. Cheng, W. Hua, J. Zhang, and W. Zhao, "Overview of stator-permanent magnet brushless machines," *IEEE Trans. Ind. Electron.*, vol. 58, no. 11, pp. 5087–5101, Mar. 2011.

[7] A. M. El-Refaie *et al.*, "Advanced high-power-density interior permanent magnet motor for traction applications," *IEEE Trans. Ind. Appl.*, vol. 50, no. 5, pp. 3235–3248, Feb. 2014.

[8] Y. Yang *et al.*, "Design and comparison of interior permanent magnet motor topologies for traction applications," *IEEE Trans. Transport. Electrific.*, vol. 3, no. 1, pp. 86–97, Oct. 2016.

[9] Z. Yang, F. Shang, I. P. Brown, and M. Krishnamurthy, "Comparative study of interior permanent magnet, induction, and switched reluctance motor drives for EV and HEV applications," *IEEE Trans. Transport. Electrific.*, vol. 1, no. 3, pp. 245–254, Aug. 2015.

[10] S. Zhu, Y. Hu, C. Liu, and K. Wang, "Iron loss and efficiency analysis of interior PM machines for electric vehicle applications," *IEEE Trans. Ind. Electron.*, vol. 65, no. 1, pp. 114–124, Jul. 2017.

[11] H. Cai, B. Guan, and L. Xu, "Low-cost ferrite PM-assisted synchronous reluctance machine for electric vehicles," *IEEE Trans. Ind. Electron.*, vol. 61, no. 10, pp. 5741–5748, Feb. 2014.

[12] M. Ferrari, N. Bianchi, and E. Fornasiero, "Analysis of rotor saturation in synchronous reluctance and PM-assisted reluctance motors," *IEEE Trans. Ind. Appl.*, vol. 51, no. 1, pp. 169–177, May 2014.

[13] T. A. Huynh and M.-F. Hsieh, "Comparative study of PM-assisted SynRM and IPMSM on constant power speed range for EV applications," *IEEE Trans. Magn.*, vol. 53, no. 11, pp. 1–6, May 2017.

[14] W. Zhao, F. Zhao, T. A. Lipo, and B.-I. Kwon, "Optimal design of a novel V-type interior permanent magnet motor with assisted barriers for the improvement of torque characteristics," *IEEE Trans. Magn.*, vol. 50, no. 11, pp. 1–4, Dec. 2014.

[15] Y. Fan, C. Tan, S. Chen, and M. Cheng, "Design and analysis of a new interior permanent magnet motor for EVs," in *Proc. IEEE 8th Int. Power Electron. Motion Control Conf.*, 2016, pp. 1357–1361.

[16] J. Y. Alsawalhi and S. D. Sudhoff, "Design optimization of asymmetric salient permanent magnet synchronous machines," *IEEE Trans. Energy Convers.*, vol. 31, no. 4, pp. 1315–1324, Jun. 2016.

[17] X. Du, G. Liu, Q. Chen, G. Xu, M. Xu, and X. Fan, "Optimal design of an inset PM motor with assisted barriers and magnet shifting for improvement of torque characteristics," *IEEE Trans. Magn.*, vol. 53, no. 11, pp. 1–4, Apr. 2017.

[18] G. Liu, G. Xu, W. Zhao, X. Du, and Q. Chen, "Improvement of torque capability of permanent-magnet motor by using hybrid rotor configuration," *IEEE Trans. Energy Convers.*, vol. 32, no. 3, pp. 953–962, Feb. 2017.

[19] G. Xu, G. Liu, W. Zhao, Q. Chen, and X. Du, "Principle of torque-angle approaching in a hybrid rotor permanent-magnet motor," *IEEE Trans. Ind. Electron.*, vol. 66, no. 4, pp. 2580–2591, Jun. 2018.

[20] F. Xing, W. Zhao, and B.-I. Kwon, "Design and optimisation of a novel asymmetric rotor structure for a PM-assisted synchronous reluctance machine," *IET Electr. Power Appl.*, vol. 13, no. 5, pp. 573–580, May 2018.

[21] H. Yang, W. Wang, H. Lin, Z. Q. Zhu, S. Lyu, and S. Niu, "A novel hybrid-pole interior PM machine with magnet-axis-shifting effect," in *Proc. IEEE int. Electr. Mach. Drives Conf.*, 2019, pp. 273–279.

[22] T. Takahashi, Y. Miyama, M. Nakano, and K. Yamane, "Permanent magnet rotating electric machine," Japan and PCT Patent Appl. WO 2019/064801 A1, Apr., 2019.

[23] K. Yamazaki and R. Kondo, "Reduction of cross magnetization in interior permanent magnet synchronous motors with V-shape magnet configurations by optimizing rotor slits," in *Proc. IEEE Energy Convers. Congr. Expo.*, 2019, pp. 4873–4879.

[24] H. Yang *et al.*, "Novel reluctance axis shifted machines with hybrid rotors," in *Proc. IEEE Energy Convers. Congr. Expo.*, 2017, pp. 2362–2367.

[25] W. Zhao, F. Xing, X. Wang, T. A. Lipo, and B.-. Kwon, "Design and analysis of a novel PM-assisted synchronous reluctance machine with axially integrated magnets by the finite-element method," *IEEE Trans. Magn.*, vol. 53, no. 6, pp. 1–4, Jun. 2017.

[26] W. Ren, Q. Xu, and Q. Li, "Asymmetrical V-shape rotor configuration of an interior permanent magnet machine for improving torque characteristics," *IEEE Trans. Magn.*, vol. 51, no. 11, pp. 1–4, Jun. 2015.

[27] Y. Jung, M. Park, and M. Lim, "Asymmetric rotor design of IPMSM for vibration reduction under certain load condition," *IEEE Trans. Energy Convers.*, vol. 35, no. 2, pp. 928–937, Jun. 2020.

[28] T. A. Burress *et al. Evaluation of the 2010 Toyota Prius Hybrid Synergy Drive System*. Oak Ridge, TN, USA, Rep.: Oak Ridge Nat. Lab., ORNL/TM2010/253, 2010.

[29] K. Yamazaki, K. Utsunomiya, A. Tanaka, and T. Nakada, "Rotor surface optimization of interior permanent magnet synchronous motors to reduce both rotor core loss and torque ripples," in *Proc. IEEE Energy Convers. Congr. Expo.*, 2020, pp. 491–496.

[30] Z. Q. Zhu and W. Q. Chu, "Advanced frozen permeability technique and applications in developing high performance electrical machines," *Trans. China Electrotech. Soc.*, vol. 31, no. 20, pp. 13–29, Oct. 2016.

[31] W. Q. Chu, Z. Q. Zhu, J. Zhang, X. Liu, D. A. Stone, and M. P. Foster, "Investigation on operational envelops and efficiency maps of electrically excited machines for electrical vehicle applications," *IEEE Trans. Magn.*, vol. 51, no. 4, pp. 1–10, Apr. 2015.

[32] B. Zhang, R. Qu, J. Wang, W. Xu, X. Fan, and Y. Chen, "Thermal model of totally enclosed water-cooled permanent-magnet synchronous machines for electric vehicle application," *IEEE Trans. Ind. Appl.*, vol. 51, no. 4, pp. 3020–3029, Jul./Aug. 2015.

[33] J. Fan *et al.* "Thermal analysis of permanent magnet motor for the electric vehicle application considering driving duty cycle," *IEEE Trans. Magn.*, vol. 46, no. 6, pp. 2493–2496, Jun. 2010.

Y. Xiao received the B. Eng. and Ph.D. degrees in electrical engineering from the Huazhong University of Science and Technology, Wuhan, China, in 2013 and 2018, respectively. Since 2018, he has been working toward the second Ph.D. degree in electronic and electrical engineering with the University of Sheffield, U.K. His current research interests include the design of permanent magnet machines.

Z.Q. Zhu (Fellow, IEEE) received the B.Eng. and M.Sc. degrees in electrical and electronic engineering from Zhejiang University, Hangzhou, China, in 1982 and 1984, respectively, and the Ph.D. degree in electrical and electronic engineering from The University of Sheffield, Sheffield, U.K., in 1991. Since 1988, he has been with The University of Sheffield, where he is currently a Professor with the Department of Electronic and Electrical Engineering, Head of the Electrical Machines and Drives Research Group, Royal Academy of Engineering/Siemens Research Chair, Academic Director of Sheffield Siemens Wind Power Research Centre, Director of Midea Electrical Machines and Control Systems Research Centres, Director of Sheffield CRRC Electric Drives Technology Research Centre. His current major research interests include the design and control of permanent-magnet brushless machines and drives for applications ranging from automotive through domestic appliance to renewable energy. Prof. Zhu is Fellow of Royal Academy of Engineering, and Fellow of IET.

S.S. Wang received the B.Eng. and M.Eng. degrees in electrical engineering from Nanjing Normal University in 2015 and Southeast University in 2018, respectively. He is currently working toward the Ph.D. degree with the University of Sheffield. His research interests include design and analysis of novel permanent-magnet machines for traction devices.

G. W. Jewell received the B.Eng. and Ph.D. degrees in electrical engineering from The University of Sheffield, Sheffield, U.K., in 1988 and 1992, respectively. Since 1994, he has been a Member of Academic Staff with the Department of Electronic and Electrical Engineering, The University of Sheffield, where he is currently a Professor of Electrical Engineering, the Head of the Department, and the Director of the Rolls-Royce University Technology Centre in Advanced Electrical Machines. He held an Engineering and Physical Sciences Research Council Advanced Research Fellowship from 2000 to 2005 and a Royal Society Industry Fellowship with Rolls-Royce from 2006 to 2008. His research interests include the modeling and design of a wide variety of electromagnetic devices, notably electrical machines for aerospace and high-temperature applications.

J.T. Chen (Senior Member, IEEE) received the B.Eng. and M.Sc. degrees from the Huazhong University of Science and Technology, Wuhan, China, in 2001 and 2004, respectively, and the Ph.D. degree from The University of Sheffield, Sheffield, U.K., in 2009, all in electrical engineering. From 2004 to 2006, he was an Engineer with Delta Electronics (Shanghai) Company, Ltd., Shanghai, China. He is currently a General Manager of Midea Automotive Components Ltd and also with the Midea Shanghai Motors and Drives Research Center, Shanghai, China. His major research interests include the design of permanent magnet machines.

D. Wu received the M.Sc. degree in electrical engineering from the Huazhong University of Science and Technology, Wuhan, China, in 2011, and the Ph.D. degree in electronic and electrical engineering from the University of Sheffield, Sheffield, U.K., in 2015. Since 2011, he has been working with the Midea Welling Motor Technology (Shanghai) Co., Ltd., Shanghai, China, and is currently Head of Motor Development Department, Welling, Midea Group. His major research interests include the design and analysis of permanent-magnet brushless machines.

L.M. Gong received the B.Eng. and M.Sc. degrees in electrical engineering from the Huazhong University of Science and Technology, Wuhan, China, in 2001 and 2004, respectively, and the Ph.D. degree in electrical and electronic engineering from the University of Sheffield, Sheffield, U.K., in 2012. From 2004 to 2008, he was with Emerson Network Power Company Ltd., Shenzhen, China, as a Research Engineer working to develop general purpose ac drives. Since 2012, he has been with the Midea Welling Motor Technology (Shanghai) Co., Ltd., Shanghai. He is currently General Manager of Servotronix Motion Control Company, Midea Group. His research interests include control of permanent-magnet brushless machines and power electronics.